Very high resolution radiometers for INSAT-2

George Joseph, V. S. Iyengar, K. Nagachenchaiah, A. S. Kiran Kumar, B. V. Aradhye, V. N. Kaduskar, R. K. Dave and C. M. Nagrani

Space Applications Centre, Ahmedabad 380 053, India

India is the first among the developing countries of the world to have its own satellites for communications, remote sensing and meteorology. The INSAT-1 series of satellites built to Indian specifications by the Ford Aerospace & Communications Corporation had the unique distinction of providing Communications and meteorological services from a single platform. These services are now being continued with enhanced capabilities through the indigenously developed INSAT-2 series of satellites. This paper describes the design, development and qualification of the Very High Resolution Radiometer (VHRR) for imaging the earth disc in the visible and thermal infrared bands from INSAT-2 for meteorological applications. Following a brief introduction to satellite meteorology, a description of the INSAT-2 VHRR instrument and the qualification process are provided. Two indigenously developed VHRRs are now operational onboard INSAT-2A and INSAT-2B and are providing weather data to the India Meteorological Department. Their ground test results and inorbit performance parameters are compared with the design specifications.

As an integral part of the multifunction INSAT-2 programme, an instrument capable of imaging earth disc in two spectral bands, from geostationary orbit, for meteorological applications was designed, developed and deployed by the Indian Space Research Organization (ISRO). This instrument is called Very High Resolution Radiometer (VHRR). This paper provides the design and development aspects of the VHRR instrument, its salient features and functions. The first part of the paper gives a brief background on the spaceborne meteorological systems. The second part provides the major design considerations, tradeoffs and a detailed description of the implemented design. The third part provides the salient performance parameters of the realized system.

Satellite meteorology

From farming to flying, weather plays a crucial role in a great variety of human activities. Meteorology is a data-intensive science, as weather is the result of several nonlinear energy transfer processes involving air, sea, land and sun. Ideally weather forecasting requires synoptic temperature, pressure, humidity and wind measurements in the atmosphere at closely-spaced points in the three spatial dimensions at frequent intervals of time and of the energy transferred through its boundaries. Supply of meteorological data has always lagged behind the requirements, despite the fact that meteorologists have pioneered operational use of new technologies almost immediately after their introduction. Thus electric telegraphy was introduced for meteorological data communication between weather data stations in 1860 and radiotelegraphy since 1905 has enabled access to weather data gathered by ships at sea. The weather aircraft, since 1918 and radiosondes since 1930 have enabled the measurements of temperature, pressure, humidity and wind at different heights in the atmosphere. By the late 1950's about 10000 ordinary land stations, 1000 sounding stations, 3000 commercial ships, 50 weather ships and several squadrons of weather aircraft were in use. Yet this network was far too sparse for monitoring weather in general and more specifically for timely forecast of severe weather conditions such as thunderstorms, cyclones etc. and it was clear that a radically different observational system was needed.

In 1947, captured V-2 rockets were used in United States to photograph the clouds from 110–165 km altitudes[1]. These first photographs demonstrated the immense potentials of observing weather from space, as the local weather was indeed seen to be a part of large-scale weather systems spread over large areas. With the satellite platform offering the possibility of gleaning very large masses of weather information, with equal ease over land and sea, routinely and at relatively low cost, planning for meteorological satellites started in right earnest in the mid-1950s.

Satellite systems used for meteorological applications can be divided into two categories, low earth orbiting (LEO) satellites and geostationary satellites. LEO satellites are characterized by better spatial resolution but limited coverage in space and time while the geostationary satellites provide better coverage at the cost of spatial resolution. The following sections present the salient features of both these categories.

Low earth orbiting satellites

The age of satellite meteorology dawned on 1 April 1960 with the launch of the experimental weather satellite

TIROS-1. It was placed in a 48.3° inclination orbit at a height of about 800 km. It carried two television cameras, one with 104° and the other with 12° field of view, imaging the earth in the visible band and mounted parallel to the satellite spin axis. TIROS-2 launched on 23 November 1960 additionally included a thermal IR scanning imager, providing for the first time the basic sensor complement of the weather satellites. The visible image of the earth provides the location and the spatial extent of the clouds against the backdrop of the earth in the sunlit portion, while the infrared image provides the temperature of the cloud tops, of the terrain and of the sea surface that is unobscured by clouds, as also the cloud extent in the day as well as the night portions of the earth. The cloud top heights are inferred from their IR temperature based on the knowledge of atmospheric height vs temperature profile. With these data, the meteorologist could locate weather fronts and storms and follow their development and movements. Until 1965, the series of eight semi-operational TIROS augmented weather observations with their data, but as these satellites in their inclined orbits precessed, daily global coverage was not possible, the time of observation varied from day to day, adding to the uncertainties and the coverage zone also shifted daily, causing large gaps in the data of any given region.

With the improvement in launch vehicle capabilities, the TIROS operational system, introduced in February 1966, enabled daily worldwide visible and IR imaging coverage with the satellites in sunsynchronous, repetitive orbits providing direct automatic picture transmission to APT receiving stations on ground as well as onboard storage of global data on magnetic tape. The TIROS operational system was spin-stabilized with the spin axis perpendicular to the orbital plane. The camera axis was mounted perpendicular to the spin axis and imaged the earth in the 'cartwheel' mode when the camera axis pointed to the nadir in the spin cycle. In the 3-axis stabilized improved TIROS operational satellite the vidicon camera of the earlier TIROS was replaced by the very high resolution radiometer providing reflected sunlight and infrared emission imaging with 1.1 km resolution, along with a vertical temperature and humidity sounder for measuring the temperature and humidity profile of the atmosphere. The current advanced TIROS-N satellites carrying a primary sensor complement of the advanced very high resolution radiometer and the TIROS operational vertical sounder have five imaging channels in visible, near IR and thermal IR with 1.1 km ground resolution, a 20-channel high resolution IR radiation sounder, an IR stratospheric sounding unit and a four-channel microwave sounding unit and thus caters additionally to applications in pollution, forest fires, volcanic eruptions, crop monitoring, reservoir level changes, ice and snow melt, ocean upwelling etc. In contrast to geostationary satellites, polar orbiting satellites have the unique capability to observe weather worldwide, including the circumpolar regions. They also transmit to relatively inexpensive APT receiving equipment. TIROS/NOAA data are received in India at 7 APT stations of the India Meteorological Department and by the National Remote Sensing Agency and have found extensive operational use in meteorology and remote sensing.

Geostationary satellites

By mid-1960s the launch vehicle capabilities reached a stage where placement of satellites in geostationary orbit became feasible. Such an orbit is ideally suited to carry out imaging operations for meteorological applications as it offers:

(i) *Continuous availability* to monitor developing and moving weather patterns and wind velocity measurements at various levels in the atmosphere using the clouds as tracers. Imaging of the earth disc is typically at 30-min intervals.

(ii) *Wide area coverage* as almost one third of the globe can be observed from the geostationary platform. To avoid large slant views in the service zone, four geostationary weather satellites are needed to monitor the weather, worldwide, between about 70° N 70° S latitude.

The first meteorological payload operated in the geostationary orbit was onboard the Application Technology Satellite—ATS-1 launched in December 1966. The payload was called the spin scan cloud cover camera (SSCC) which generated the imagery of the earth in the visible spectrum. Since then a number of countries have been operating geosynchronous earth observation satellites for meteorological applications. These include GOES by USA, GMS by Japan, Meteosat by Europe, GOS by USSR and INSAT by India.

Imaging systems on geostationary platforms: For meteorological applications, the spaceborne sensors can be broadly classified as (i) imagers and (ii) sounders. The sounders provide information on the vertical distribution of certain parameters of meteorological importance like temperature, humidity etc. In this article, we will be dealing with the imager type of instruments. All the geostationary satellite systems mentioned above carry an imaging instrument—very high resolution radiometer—to image the earth disc in visible and thermal IR bands. (Meteosat provides imaging in the water vapour band also). Table 1 gives a comparative summary of various VHRR instruments.

It is interesting to note that except INSAT, which is a 3-axis stabilized system, all the other spacecraft in geostationary orbit conducting meteorological observations on an operational basis are spinners. (Drawing from INSAT experience the next generation GOES series of satellites of NOAA are being developed as 3-axes

Table 1. Comparison of VHRR instruments onboard geostationary satellites

	METEOSAT	GOES	GMS
Telescope diameter (cm)	40	40 6	40 6
Scan system	Spacecraft spin motion plus telescope tilt	Spacecraft spin motion plus scan mirror	Spacecraft spin motion plus scan mirror
Spin rate (rpm)	100	100	100
Wavelength (µm)			
IR	10.5–12 5	10.5–12.5	10.5–12 5
VIS	0.4–1 1	0 55–0.75	0 55–0.75
Other channels			
WV	5.7–7.1	12 6, 7.2, 6.7	–
CO_2	–	4 4–4 5, 13.3–14.7	–
Detectors			
IR	HgCdTe	HgCdTe/InSb	HgCdTe
VIS	Si	PMT	PMT
Subsatellite resolution (km)			
IR	5	6.9	5
VIS	2.5	0 9	1.25
NEDT IR	< 0.4 K at 300 K	0.11 K at 300 K	< 0.5 K at 300 K
S/N	> 4 : 1 at 0.5% albedo	2.5 : 1 at 0.5% albedo	> 1.4 : 1 at 0.5% albedo
Image viewing angle (deg)	18 × 18	20 × 20	18 × 18
Sector	–	Full E-W coverage with programmable N–S coverage	–
Frame time (min)	25	30	30

stabilized systems). Since the satellite position remains stationary with respect to earth in a geostationary orbit, the spin of the satellite produces one scan line in the west-east direction. North-south scanning is carried out by stepping the scan mirror placed in front of the entrance aperture of the telescope. In the case of Meteosat, the entire telescope is stepped at the end of each east-west scan to scan in the north-south direction. The satellite is generally spun at about 100 rpm and images the earth once every 30 minutes. The efficiency of scanning is very poor (~ 5%), as the earth subtends only about 17° from the geosynchronous orbit and the instrument sees the deep space during the rest of the rotation period. This necessitates larger collecting optics and also results in higher data rate compared to an instrument placed on a 3-axes stabilized platform. However, spinners have the advantage of better spacecraft stability due to the rigidity of the spin axis and better thermal environment due to the averaging of the heat

input. In the case of a 3-axes stabilized system, by employing bi-directional scanning, scan efficiency as high as 80–85% can be achieved. Due to this, for comparable performance, VHRR instrument onboard the 3-axes stabilized platform can use 8″ optics against 16″ optics used by spinners and signal bandwidth requirement is correspondingly lower, resulting in better signal to noise ratio.

The INSAT very high resolution radiometer

The INSAT programme

As a part of the application-driven Indian space programme, the Indian National Satellite, INSAT, catering to the needs of broadcasting, television, telecommunications and meteorology was conceived in the 1970s. The first generation INSAT satellites (INSAT-1A to 1D) were built by the then Ford Aerospace and Communication Corporation, USA, to the Indian specifications. Each INSAT-1 satellite carried a communications payload of 12 C- band transponders and two S-band transponders, and a meteorological payload composed of a very high resolution radiometer (VHRR) which images the earth in visible (0.55–0.75 µ) and thermal infrared (10.5–12.5 µ) spectral bands; and a data collection platform transponder to collect and transmit meteorological data from unattended ground-based platforms.

The ground resolution of the INSAT-1 VHRR at the subsatellite point for nadir view is 2.75 × 2.75 km in the visible and 11 × 11 km in the IR band. The first satellite of the series, INSAT-1A was launched in April 1981 followed by INSAT-1B in August 1983, INSAT-1C in July 1988 and INSAT-1D in July 1990. Currently INSAT-1D is operational.

The second generation INSAT satellites (INSAT-2 series), which have to cater to the growing demands—both in terms of quality and quantity—of user community till the turn of the century have been designed and built indigenously by ISRO. The first of the INSAT-2 series satellites (INSAT-2A) was launched on 10 July 1992 and the second satellite (INSAT-2B) was launched on 23 July 1993, by Ariane-IV launchers, and they are currently providing operational communications and meteorological services to the country. The VHRR instruments onboard INSAT-2 are of improved spatial resolution. The ground resolution of INSAT-2 VHRR at the sub-satellite point is 2 × 2 km in the visible band and 8 × 8 km in the IR band. INSAT-2A is stationed at 74° E longitude and INSAT-2B at 93° E longitude.

The INSAT-2 VHRR can be operated in any one of the following modes (Figure 1): (a) Full scan mode covers the entire earth disc and some space around in 33 minutes. (b) Normal scan mode covering atleast 50°N to 40°S latitude can be imaged in about 23 minutes. (c) Sector scan mode in which the sector can be positioned anywere in the earth disc along N–S direction

FULL SCAN

NORMAL SCAN

SECTOR SCAN

* HATCHED REGION INDICATES THE IMAGED AREA DURING SCAN

Figure 1. Scan modes of INSAT-2-VHRR

takes about 7.2 minutes. This mode is particularly suited for rapid repetitive coverage of the scene during severe weather conditions like cyclones.

The major performance parameters required to be met by the instrument are given in Table 2.

System description

Figure 2 gives a simplified block schematic of the VHRR instrument. It is organized into three packages: The electro–optics (EO) module, electronics package–1, and electronics package–2. The EO module houses the scan mechanism assembly, the optics assembly and the radiant cooler assembly. The visible detector and pre-amplifier and the IR detector and preamplifier are also mounted in the EO module. The electronics package–1 contains the signal processors for all the channels, data formatter, power distribution, and timing logic circuits. The electronics package–2 houses the scan mechanism

Table 2. Specifications of INSAT-2A VHRR

Spectral Bands	
(a) IR channel	
1. Band (μ)	$10.5 \pm 0.2 - 12.5 \pm 0.2$
2. Integrated out-of-band response (%)	< 3
3. Out-of-band response peak (%)	< 0.1
(b) Visible channel	
1. Band (μ)	$0.55 \pm 0.04 - 0.75 \pm 0.04$
2. Integrated out-of-band response (%)	< 3
3. Inter detector mismatch (%)	< 5
Resolution	
IR IFOV (km/μrad)	8/223
Out of field response (%)	< 2
VIS IFOV (km/μrad)	2/56
Out of field response (%)	< 2
Radiometric performance	
IR channel NEDT at 300 K	< 0.25 K
Visible channel SNR at 2.5% albedo	> 6
Dynamic range	
IR channel dynamic range (K)	4–340
IR channel nonlinearity (%)	< 1
Visible channel dynamic range (%)	
albedo	0–100
Visible channel nonlinearity (%)	< 2
Misregistration	
Between VIS & IR channels (μrad)	< ± 56
Modulation transfer function	
IR channel (%)	> 21
Visible channel (%)	> 23

electronics, all the DC/DC converter regulators, patch temperature controller and the analog telemetry processor.

Optical subsystem

The VHRR optics is depicted schematically in Figure 3. Since the instrument has to cover a broad spectrum in two widely separated wavelength regions, 0.55–0.75 μ and 10.5–12.5 μ, an all reflective telescope system was chosen for the collecting optics. The incoming radiation from the scene is reflected onto the 8" aperture of an Ritchey-Chretien (R–C) telescope by a beryllium scan mirror(m) which is mounted at 45° to the optical axis of the telescope. Minimization of volume and weight calls for the use of a 'folded' optical system. Figure 4 shows the geometric spot size as a function of the field angle for different telescope configurations. From the various types of such telescopes, the R–C configuration was chosen, considering its ability to provide the relatively large field of view (about 0.1°) necessary for accommodating redundant detector sets within the high performance zone in the focal plane.

The primary mirror (a) of the telescope is a concave hyperboloid in shape with a clear aperture of 202 mm and f/2.0. The secondary mirror (b) is a convex hyperboloid with an aperture of 62 mm. The separation between the primary and secondary mirrors is about
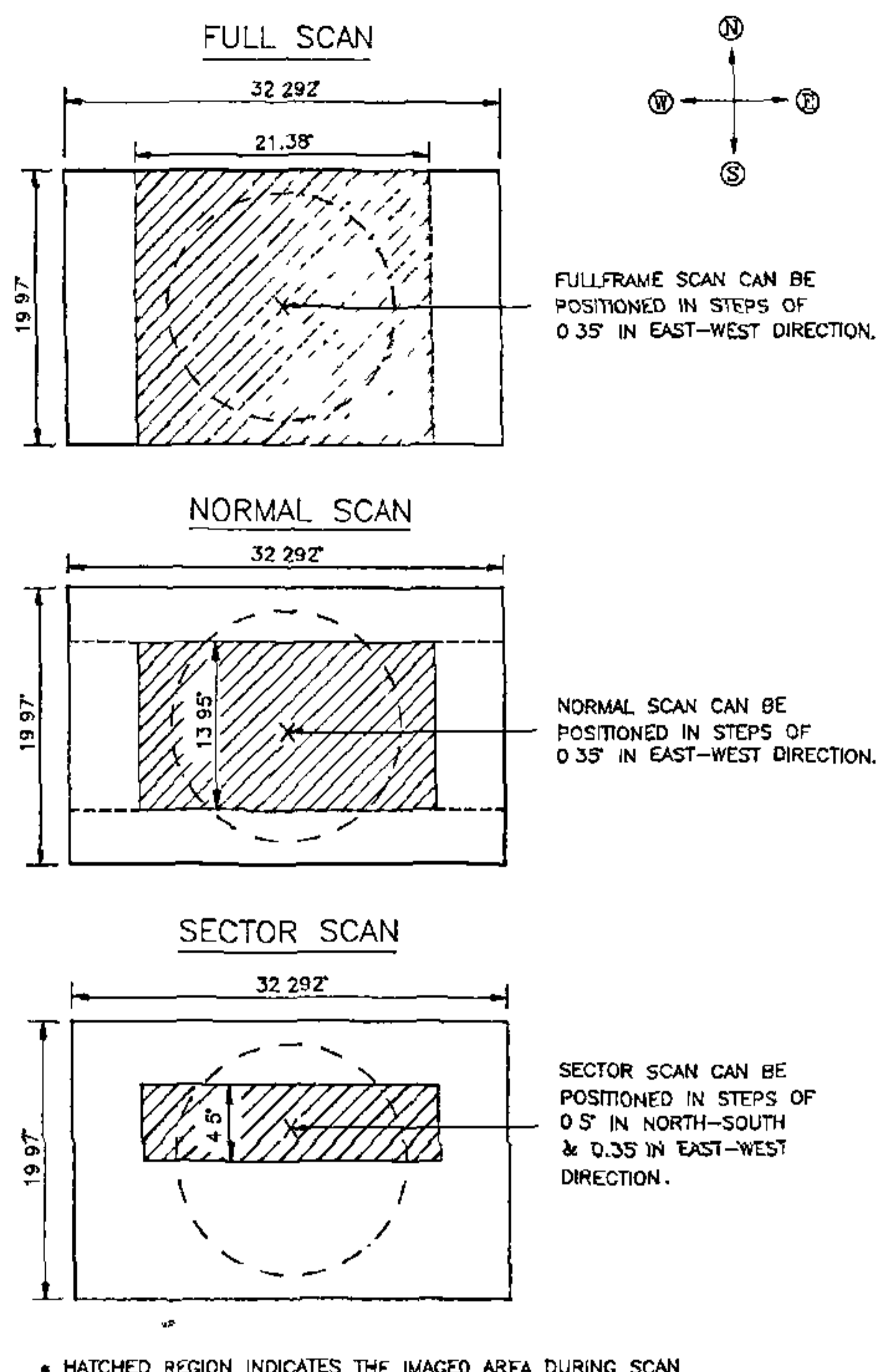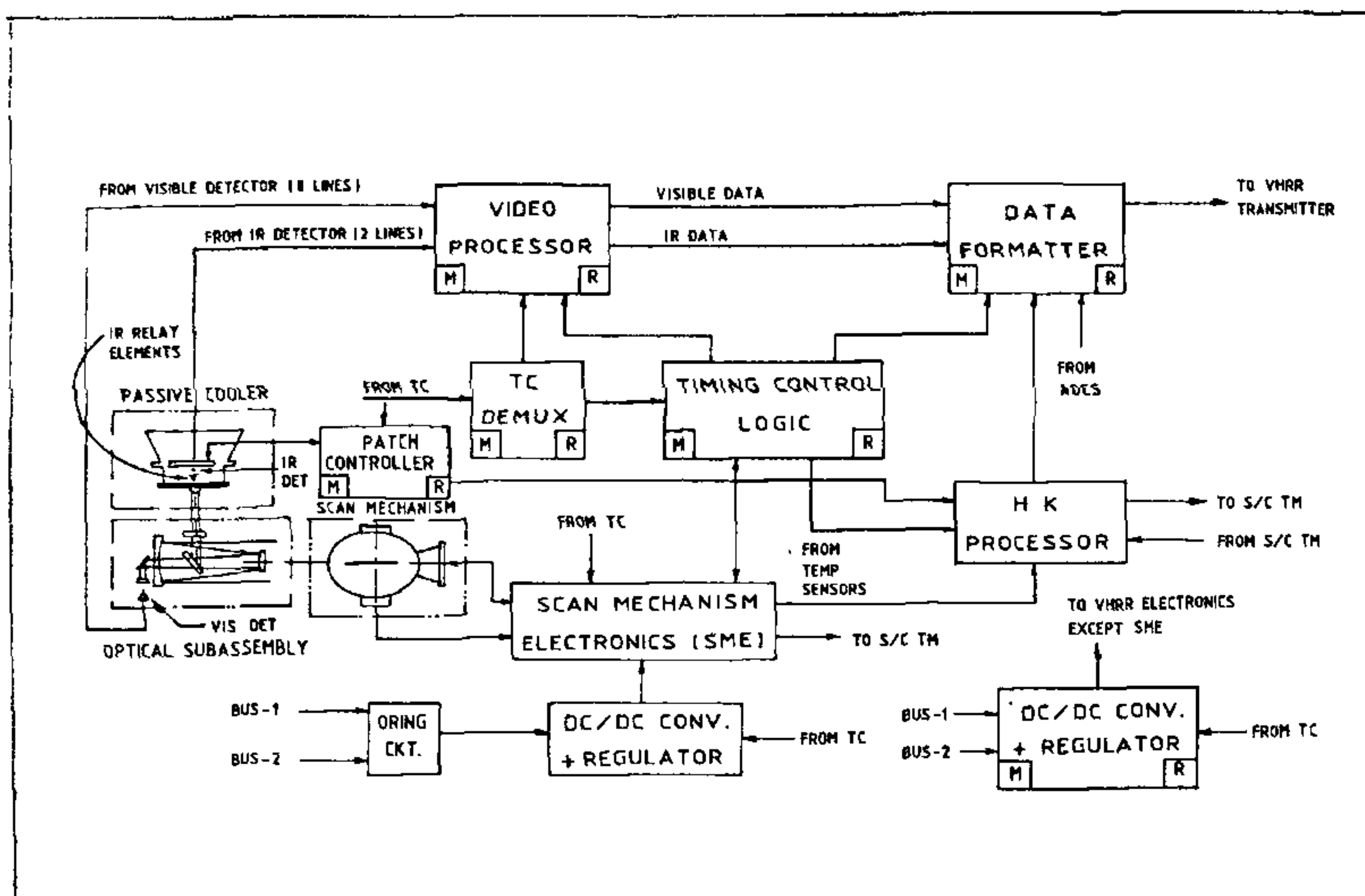
45

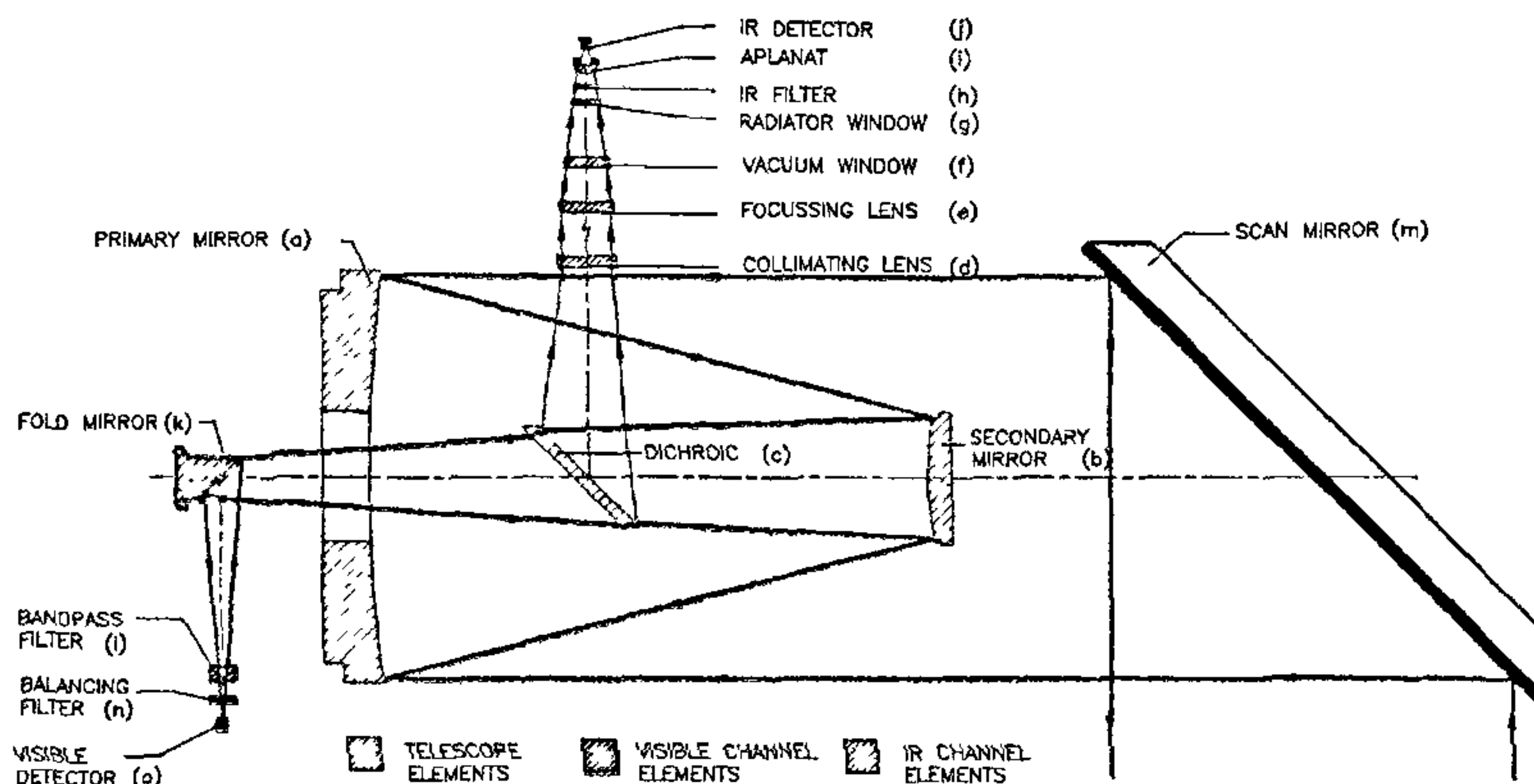Figure 2. INSAT-2 VHRR-simplified block schematic

Figure 3. Optical schematic of INSAT-2-VHRR.

285 mm. The effective focal length of the system is 1594 mm.

Mechanical design ensured that the relative positions (separation and concentricity) and tilts between various optical elements are maintained within very close tolerances, under dynamic environment, without stressing the optical elements beyond their microyield strength. Hence

clamping and locking methods had to be specially evolved. All the optical elements were hard mounted in metallic mounts to have stable reference surfaces. Uniform distribution of clamping force over the optical component was achieved by using flat gasket-type rings of viton between the optical element and its lock ring. The maximum allowable hold down torque for each of

46

FOCAL LENGTH = 1594 mm

FOCAL NUMBER = 7 85

GEOMETRIC SPOT SIZE CORRESPONDS TO 90% ENERGY
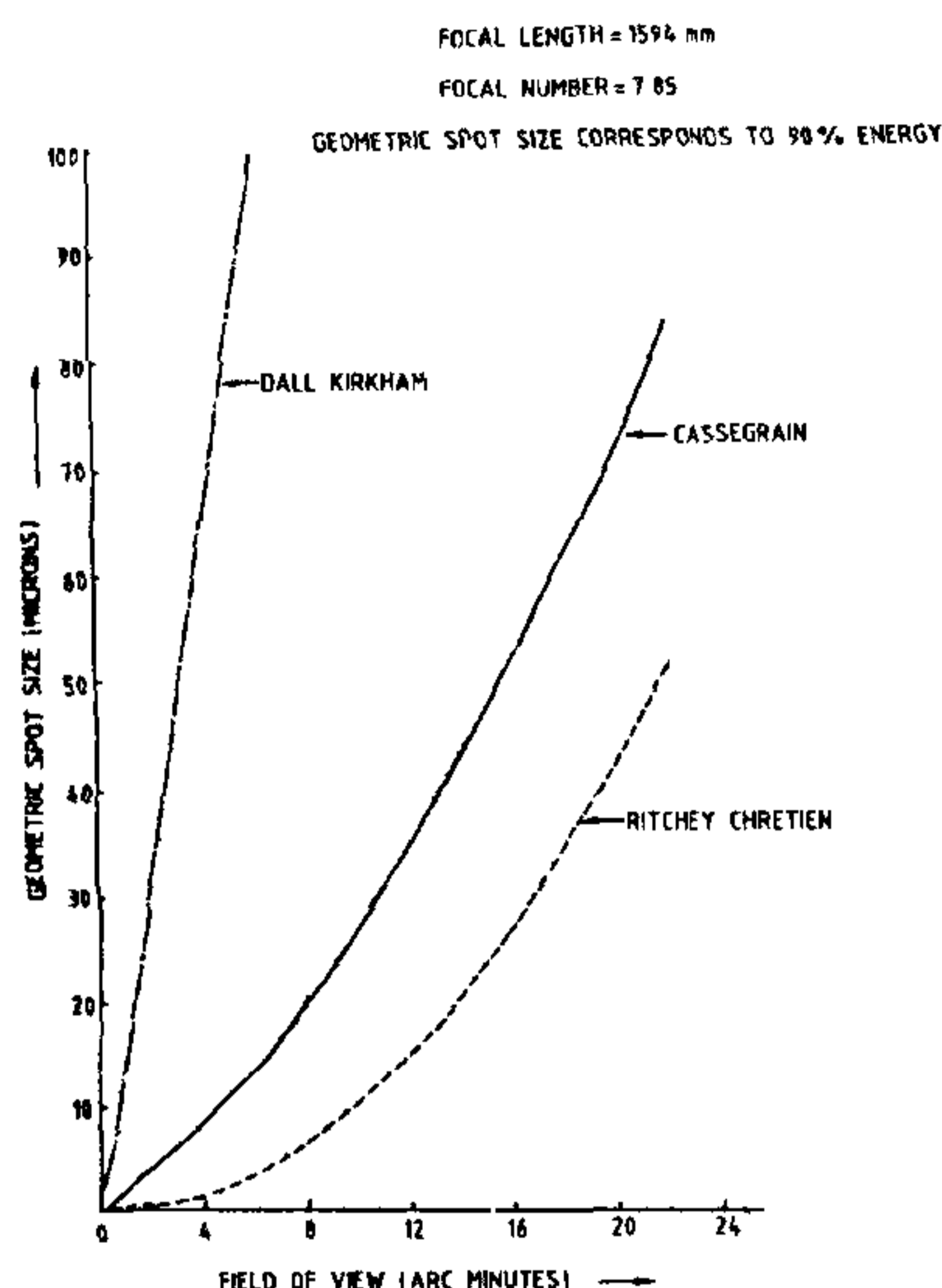
Figure 4. Geometric spot size as a function of field–A comparison

element was determined experimentally by interferometrically observing the distortion of the optical surface. These torque values are significantly lower than those normally adopted for similar sizes in general engineering practice. Therefore adhesives were used to prevent loosening of threaded rings under dynamic loading conditions. For heavier and larger parts, like the primary mirror and the secondary mirror mount, antirotation pins/screws were used to prevent possible rotation of the elements due to vibrations. The all-invar telescope housing ensured nearly athermal performance over the operating temperature range of 0 to 50° C.

The convergent light beam (f/7.85) reflected from the secondary mirror is incident on the dichroic beam splitter (c) which is mounted at 45° to the telescope axis. This surface of the beam splitter is optically flat and is coated with a very thin evaporated gold layer giving 85% reflectance in IR and 74% transmission in visible band. Figure 5 depicts the reflectance/transmittance of the dichroic mirror as a function of wavelength. The dichroic beam splitter was fabricated from fused silica, chosen to provide high mechanical strength and low coefficient of thermal expansion. As the beam splitter is in the transmission path in the convergent beam of the visible channel, it is a potential source of wavefront aberration. This is compensated by shaping the second surface of the beam splitter to have a wedge of angle

about 11° with a superposed spherical surface of radius of curvature of 67500 mm. The transmitted light is then reflected onto the visible detector by a fold mirror (k). This fold mirror serves to reduce the length of the optical module. The reflected light from the fold mirror passes through the spectral balancing (l) and band pass filter (n). The dichroic and the fold mirror are housed in a tripod assembly made of invar. The tripod is fixed to primary mirror mount to achieve the required positional accuracies. The visible channel tube, housing the filter and the detector, is also mounted on the tripod assembly. The entire telescope assembly is fixed onto the telescope mounting frame of the EO module.

The reflected IR radiation from the dichroic reaches a zinc selenide lens (d) mounted on the side of the telescope barrel which collimates the IR beam. The collimated output, in effect, is that of an afocal telescope with an eightfold reduction in beam aperture from 200 to 25 mm and is incident on the zinc selenide IR focus lens (e) mounted on the passive radiative cooler which converges the beam to f/4.7. The beam then passes through a ZnSe vacuum window (f), a cooled band limiting radiation window (g) to reduce the heat input to cooler, a band pass IR filter (h) and is finally speeded up to f/1.1 by a germanium aplanat lens (i) to form the 8 km resolution image on the $33 \times 33\,\mu$ mercury cadmium telluride detectors (j), cooled by the passive radiative cooler to a nominal temperature of 105 K.

Passive radiative cooler subsystem

The three-stage passive radiative cooler[2] consists of four main components : patch, radiator, vacuum housing and sun shields. The patch is supported through thermal insulators from the radiator which in turn is similarly supported from the vacuum housing. The IR detector is mounted on the patch. The cooler is mounted on the spacecraft with the patch facing north. The sun shield protects the patch from the direct rays of the sun. The surface of the sun shield facing the patch is made highly specularly reflective so as to minimize the heat load from sun shield onto the patch. The internal surfaces of the radiative cooler are gold-plated to inhibit radiative heat transfer between the housing, radiator and patch. The space viewing surface of the patch is a blackened honeycomb while that of the radiator is white-painted. The patch temperature controller consisting of platinum resistance thermometers (PRT) as sensors and thermofoil heaters as actuators maintain the patch temperature at the set point. The patch temperature can be set to any value in the range of 105–115 K in steps of 1.4 K and is controlled to an accuracy better than 0.1 K. Heaters are fixed on the patch, radiator, vacuum housing and sun shields of the cooler to heat up these parts during decontamination mode to facilitate out-gassing and to prevent the condensation of the contaminants during the initial mission phase. The temperatures of various parts
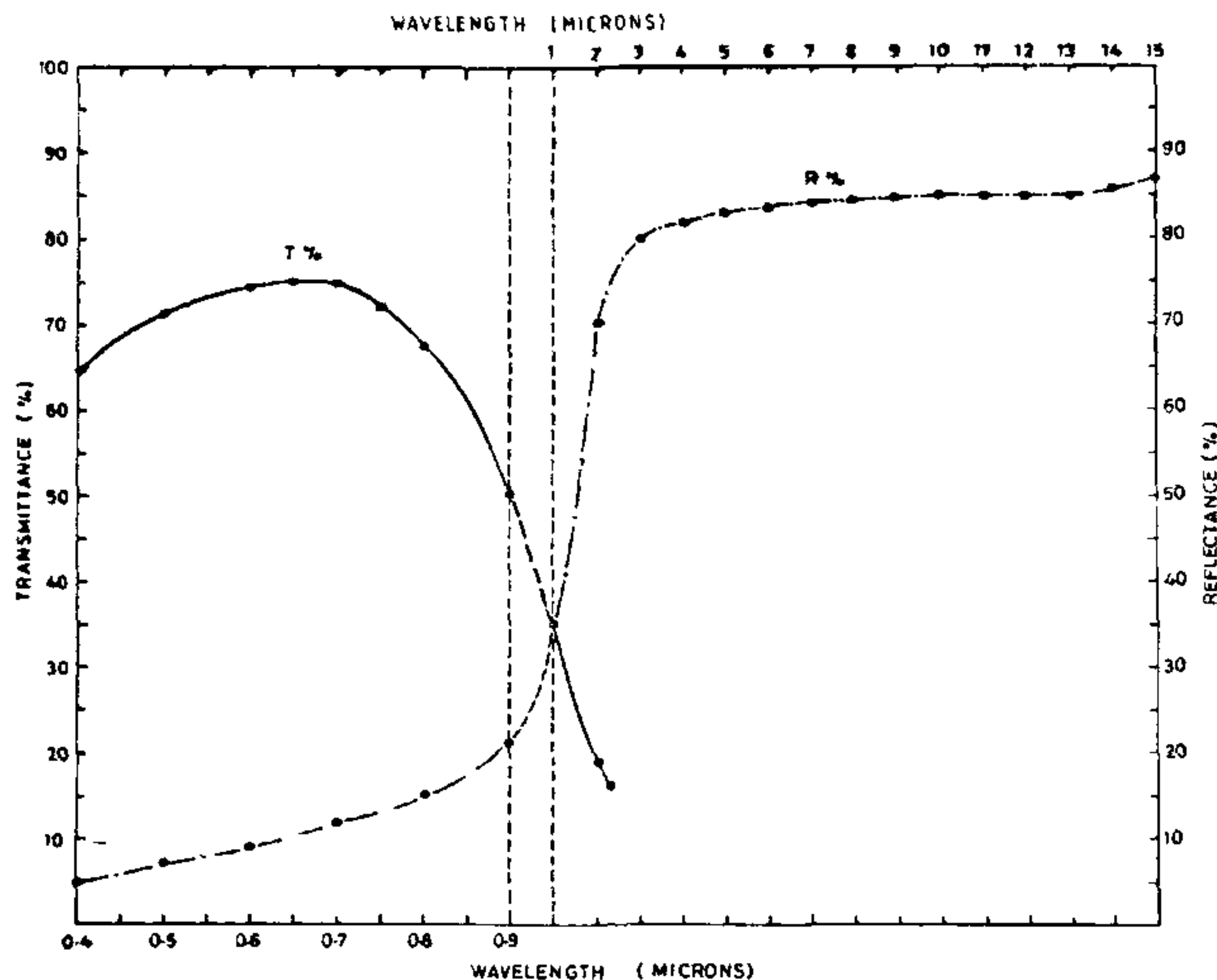
47

Figure 5. Dichroic transmittance and reflectance curves.

Detector subsystem

of the cooler are measured using PRTs and monitored through the VHRR telemetry.

The visible channel radiation is directed to two arrays of 4 silicon photodiodes each providing a 2 km resolution at the nadir. The system design requires the use of four element detector assembly to reduce the scan mirror oscillation frequency to about 1 Hz. To provide redundancy in case of failure or degradation, four more detector elements are included in the same detector package. To improve the collection efficiency and reduce the impact of cross-talk on radiometric and geometric performance, the four elements are staggered in the fast-scan direction (see Figure 6). In contrast to a linear array, a staggered array permits the imaging without any underlap in the N-S scan direction and thus maximizes the signal and through the physical separation, minimizes the cross-talk between the adjacent detector elements. The detector element active area and the focal length of the optics together determine the instantaneous field-of-view (IFOV) of the instrument. The chosen active dimension of the detector is 85 x85 μ. The detector responsivity is optimized for use in the wavelength band of 0.55–0.75 μ. The metal mask of the visible detector was specially designed to minimize the out-of-field response and maximize the modulation transfer function (MTF). The eight-element silicon photodetector is housed

in a low profile TO-5 package with a sapphire radiation window.

The IR detector assembly consists of two HgCdTe photo-conductive detectors which are housed inside the passive radiant cooler. The IR detector needs to be
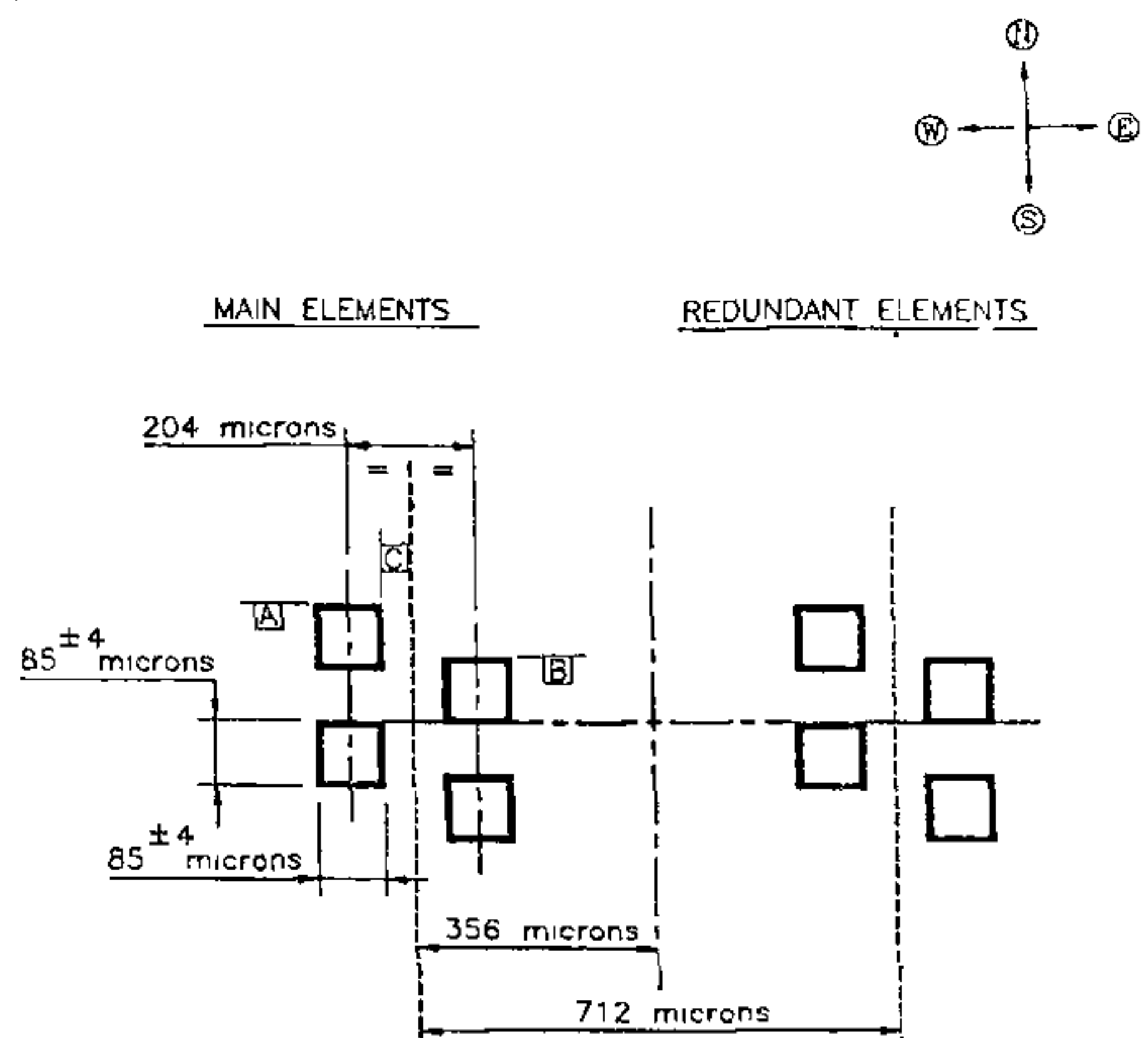

Figure 6. Visible focal plane

operated at very low temperatures to get the required noise equivalent temperature difference (NEDT) measurement capability. The detector is operated at 105 K. The active size of the detector is a critical design parameter as it affects the IFOV, the noise performance and the signal collection capability. The element size chosen is 33 x 33 μ (see Figure 7). Since the IFOV of the IR channel is four times larger than visible IFOV, one detector element is adequate. Redundancy is provided by having one more element in the same package. The detector package is designed to include a germanium aplanat lens and IR band pass filter so that these two components also are at the same temperature as the detector, thus reducing the background signal and the associated noise. The HgCdTe composition is optimized for peak performance in the wavelength region of 10.5–12.5 μ when used in the temperature range of 105–115 K.

Scan mirror subsystem[3]

The scan mirror(m) which is mounted on a two-axis gimballed scan mechanism generates two-dimensional images by sweeping the detector instantaneous field-of-view in the east-west and north-south directions. In each E-W/W-E scan one IR scan line of 8 km width and four visible band scan lines, each of 2 km width are generated. The scan mechanism enables the instantaneous field-of-view of VHRR instrument to be scanned over the earth scene covering 21.4° along east to west and 20° along north to south. This is achieved by moving the beryllium scan mirror about two axes (fast scan in east west axis and slow scan in north south axis) which are perpendicular to each other. Fast scan and slow scan motions of the mirror are controlled by separate servosystems consisting of an inductosyn angle encoder,

a d.c brush-less motor and servo electronics. To achieve the uniform scan rate, the servo makes the mirror to follow a predefined reference. Good linearity and repeatability are ensured using a precision servo loop. The servo motions are slaved to the VHRR bit rate clock so that the mirror motion is synchronized with the data acquisition system.

The scan mirror is required to move ±5.35° about the fast scan axis and ±10° about the slow scan axis to provide a full frame coverage of 20 x 21.4°. The scan mirror takes about 1 s, to cover the fast scan, at the end of which the scan direction is reversed and the mirror is stepped in the slow scan direction by one IR IFOV of 223 μ rad. The turn around of the scan mirror is achieved smoothly by reducing the scan rate to half, one fourth and finally to zero speed and then increasing it in similar steps in the opposite direction.

The scan mechanism enables operation of the VHRR payload in three modes namely, full frame mode, normal frame mode and sector mode. A fast scan offset capability enables the ±10.7° scan to be positioned in a ±15° field to take care of satellite orbital position anywhere between 70° E and 100° E. In sector scan mode it is possible to select any one of 32 sectors in steps of 0.5° in N-S direction by telecommand. At the end of each full frame or normal scan, the mirror turns by 90° to view the black body calibration source. In the sector mode the black body calibration is carried out only on command.

The scan mirror should have high dimensional stability to maintain its optical flatness throughout its lifetime under thermal gradients in the instrument and the clamping stresses. This calls for judicious selection of material, special clamping techniques and suitable configuration of the structure. The scan mirror is made of beryllium due to its low density, high specific heat, high thermal conductivity and low Poisson's ratio, high strength, stiffness and high dimensional stability. The 340 x 210 mm elliptical scan mirror is 19 mm thick and weighs 800 g. The rear surface of the mirror carries weight relieving square cavities leaving a front skin of 3 mm thickness. Stress relief grooves are provided at mounting pads on the back surface of the mirror to inhibit transfer of mounting stresses to the front surface of the mirror. Stiffness of the mirror is greater than that of the pads. The mirror mounting surfaces are maintained coplanar and optically flat. Mechanical limit stops provide the mechanical initialization reference for fast and slow scan axes, required for reproducible scans.

Figure 7. IR focal plane.

Electro optics module

The optical elements, scan mechanism and the passive radiative cooler are housed in the electro-optics module which is a box-shaped structure of size 870 x 325 x 325

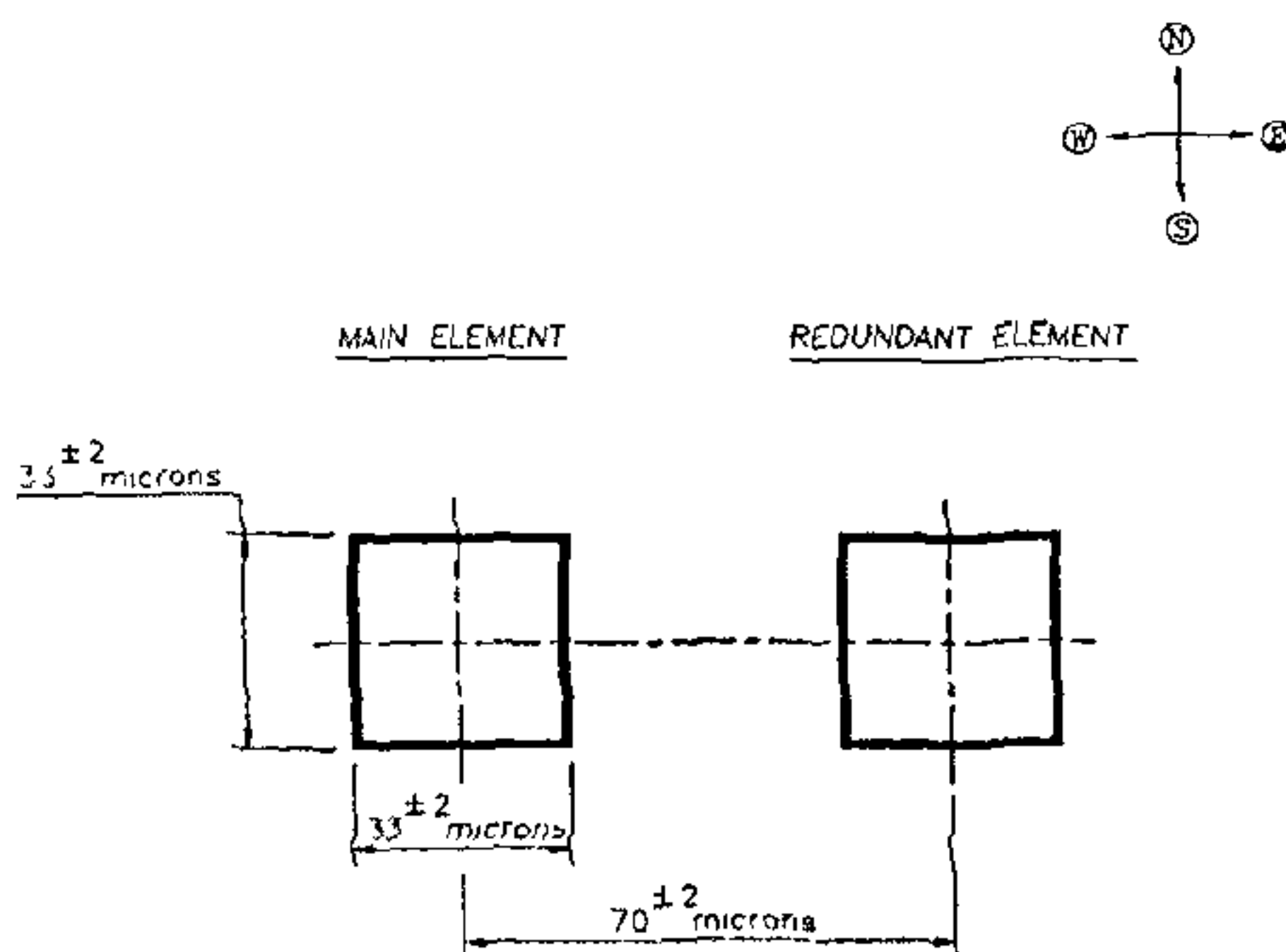mm. Two bulkheads, one each on either side of the cooler location, are provided to impart adequate structural stiffness. One of them supports the telescope assembly in cantilever mode. Three stud-like supports are provided to limit the deflection of the free end of the telescope under launch environment. All the six sides and two bulkheads are made out of aluminum alloy 6061-T6 plates. About 80 to 90% of the material is selectively scooped out leaving a membrane with suitable stiffening ribs and skirting on four sides. Dowels are used between the mating parts to provide a stable base for mounting the three subassemblies, viz. the scan mechanism, the telescope and the cooler. The base plate of the structure provides the interface with the spacecraft through six mounting lugs integrally machined on the base plate. Coplanarity of the surface of these lugs is achieved by machining these in the assembled condition of the structure.

Electronics subsystem

The major functions of the electronics (Figure 8) are: (a) Amplify, DC restore and digitize the detector outputs (video signal processing). (b) Control temperature of IR detectors mounted on passive radiant cooler. (c) Generate master clock and other logic control pulses. (d) Format, encode and randomize the digital data stream. In addition, the electronics monitors and formats the various housekeeping data and interfaces with the spacecraft subsystems.

Visible channel preamplifier: The VHRR electronics processes the detector signals and provides detector and quantization limited noise performance commensurate with the requirements of radiometric resolution.

The visible channel pre-amplifier is a transimpedance amplifier. At low frequencies the transimpedance can be approximated by feedback resistor (Rf). The thermal noise due to Rf is the dominating source of noise, and the signal-to-noise ratio is proportional to the $\sqrt{Rf}$. However, the maximum value of feedback resistor is limited to 30 M by bandwidth requirement in the presence of the layout and stray capacitance of the order of 1 pF.

Based on the resolution and the scan rate, the required channel bandwidth is DC to 3.2 kHz and is set by a low pass filter, just prior to A to D converter. The equivalent input noise of the visible preamplifier is less than 0.55 pA RMS.

IR channel pre-amplifier: The IR channel detector is biased for operation in photoconductive mode with a bias current of 2 mA. The biasing of the detector results in large offset voltage and introduces another source of noise. With 70 ohm typical detector resistance, 1 mV full scale signal from the detector is superimposed on 140 mV offset. Further, the dark resistance of the detector varies by ± 4 ohm over the temperature range of 105–115 K, generating ± 8 mV offset at the amplifier input. The detector, along with its biasing and compensating resistors, is connected in a bridge configuration to give symmetrical bipolar offset in the envisaged operating environment. The pre-amplifier is a differential amplifier with a pair of low noise supermatched transistors forming
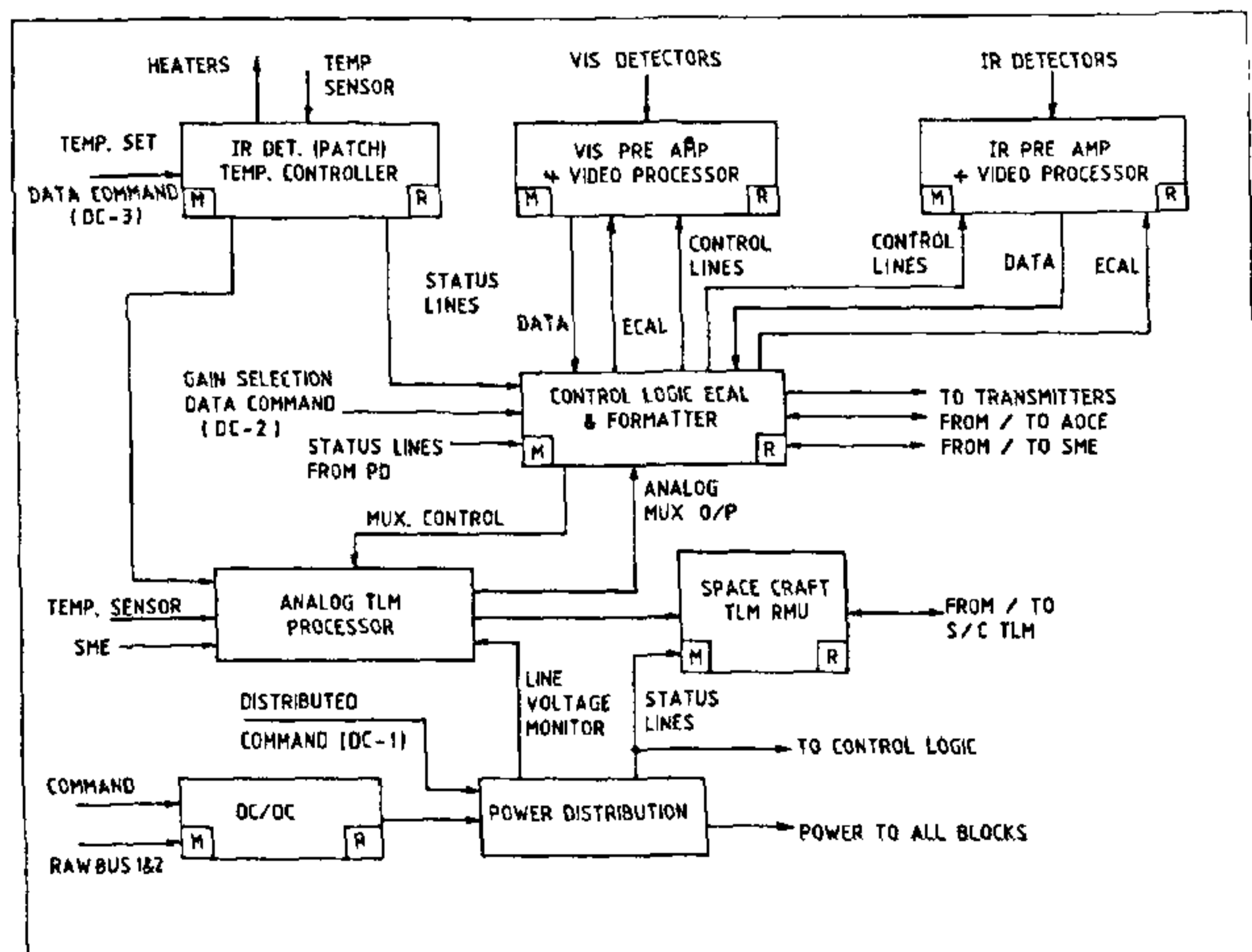

Figure 8. Camera electronics block schematic.

the input stage and provides a gain of 160. The pre-amplifier noise is mainly due to the input voltage noise of the matched pair and the thermal noise of bias resistors and works out to be 50 nV. Thus, the noise performance of detector and pre-amplifier combination is essentially limited by the detector noise of ≈ 100 nV RMS.

DC restoration/clamping: The pre-amplifier output offset is at least an order of magnitude higher than the full scale signal. This offset is removed prior to the signal amplification to utilize the full dynamic range of ADC. DC restoration scheme wherein space view reference signal is stored in a capacitor and subsequently subtracted from the scene video is not suitable for the low refresh rates involved. The realization of clamping requires 400 µF capacitor to limit the droop to less than 0.025%. To circumvent this problem, the reference during space view is digitized, stored and subtracted to get the true scene signal. The magnitude of the offset is such that significant signal amplification is needed after offset subtraction whereby any error in the estimation of the offset is also amplified. To overcome this problem, offset digitization is done in two steps. In the first step, the offset is applied to the ADC with an amplification such that the maximum possible value of the offset is within the dynamic range of ADC. The digitized value of the offset is stored in a register-DAC combination, and is called coarse-clamp value. This is next substracted from the actual offset to estimate residual offset. After suitable amplification and digitization, this residue is stored in another register–DAC combination and is called fine-clamp value. During mirror scan, both coarse and fine clamps are subtracted from the composite video, after proper amplification/attenuation, and the signals are offset so that dark/deep space scenes give a non-zero count.

IR detector temperature control: The IR detectors, mounted on the patch of the passive, radiative cooler, are operated at controlled low temperature to get optimum performance. The patch temperature is controlled precisely using PRT sensors and heaters mounted on it. The controller is of ON/OFF type with PRT sensors as feedback elements and heaters as actuators. It has two operational modes viz. IR operation mode and the decontamination mode. The IR operation mode is the nominal mode of operation, wherein the patch is maintained at the controlled low temperature. The temperature sensor output is conditioned and digitized with resolution better than 0.1 K. The digitized value is compared with the set point values to decide on the ON/OFF state of heater. The decision process is repeated every second and a fixed quantum of energy is given to the heater in case the heater is switched on. The set point value can be changed in eight steps over the range of 105–115 K through a data command.

The decontamination mode operation is similar to that of IR mode except that the set point values are near 300 K. The resolution is correspondingly poorer and the quantum of energy per heater activation is larger than the IR mode of operation.

It is not advisable to extend bias to the IR detector except at cryogenic temperatures. In order to protect the detector from inadvertent operation at higher temperature, the detector bias is controlled by the patch temperature. The detector bias is switched on, only when the patch temperature is less than 125 K and the controller is not in decontamination mode. The data command can be used for overriding the inhibition of detector bias and defeating the control function to monitor the patch temperature.

The patch temperature controller has complete functional redundancy. In addition, any one of the two heaters on the patch can be used as actuators with either of the controllers.

Control logic and formatter: This digital system serves as the master controller for the instrument. It generates bit rate clock at 526.5 kHz and provides the basic timing signals to all the other subsystems. In addition, it generates various control signals for data acquisition, processing, DC restoration, A/D conversion and the electrical calibration signal generation for video processors. The formatter takes data from the video processor, scan mechanism and analog/digital telemetry circuits and inserts the same in the instrument output stream along with the frame sync code. Odd parity is inserted for every 99 bits. The telemetry data include information related to spacecraft attitude, sensor configuration, subsystem health, clamp and electrical calibration etc., required for image reconstruction and performance evaluation. The data format with respect to number of lines in a frame depends on the scan mode selected. Each line consists of 6500 data blocks of 100 bits each. In the absence of scan, the information is replaced by pseudo random binary sequence. The final output is given to the transmitters in randomized NRZ-S code and is transmitted in the extended C-band.

System integration and testing

The VHRR payload integration was carried out in stages to facilitate parallel development of different subsystems. The sub-assemblies were so demarcated as to enable independent verification and performance optimization at subsystem level such as telescope, scan mechanism, passive cooler, visible channel, infrared channel, electro optics module and the electronics packages. A number of test facilities like visible/infrared detector evaluation set-up, scan mechanism evaluation set-up, bench cooler set-up, MTF test bench, spectral response test bench, payload evaluation set-up and computer-aided VHRR evaluation system (CAVES) were developed to optimize and evaluate the final performance of the system.
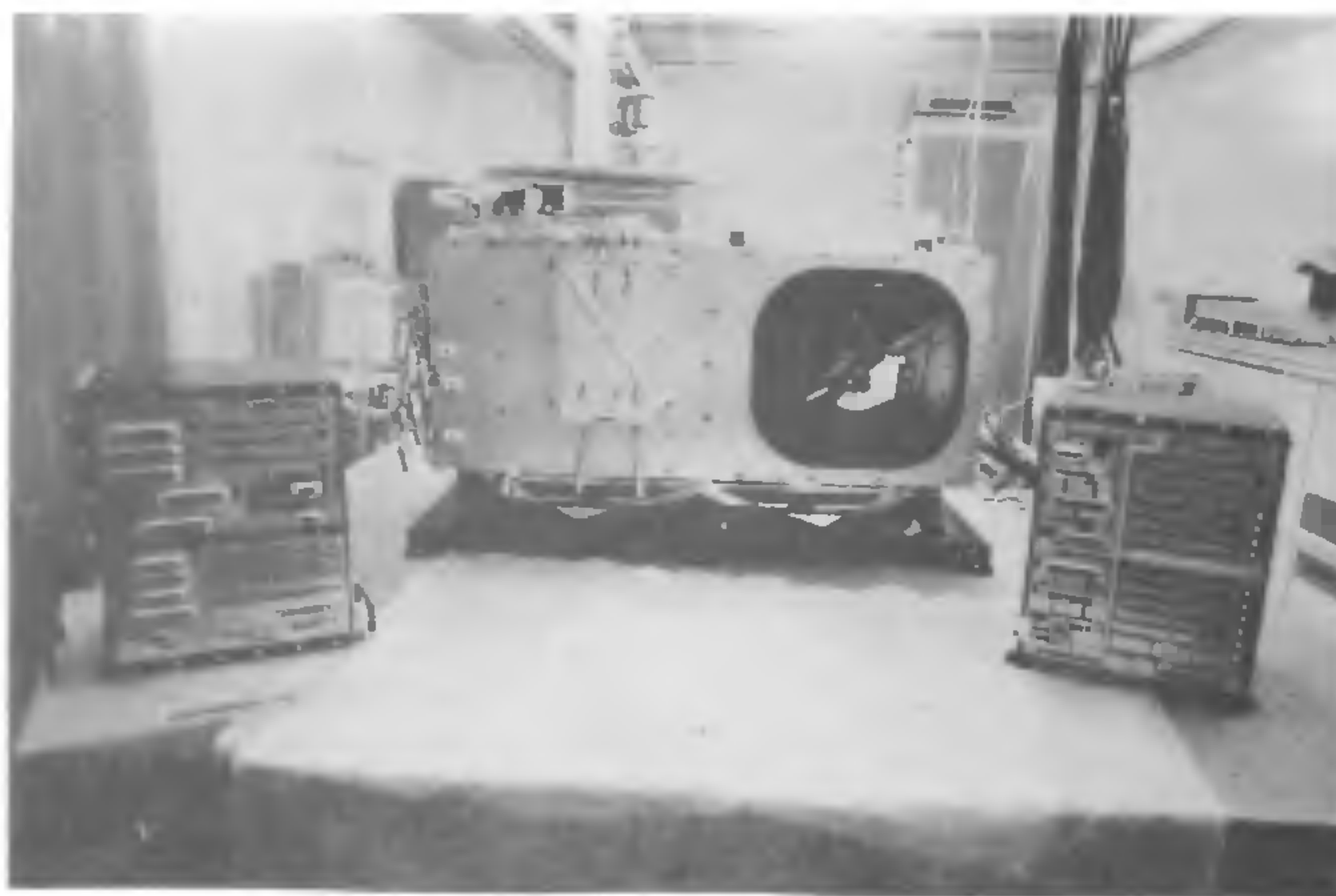
To ensure adequate design margins in the performance

Figure 9. INSAT-2 VHRR flight model instrument.

of the instrument during/after exposure to severe thermal and mechanical environment the instrument was likely to encounter during launch, transfer orbit phase and in the synchronous orbit, a structural model and engineering thermal model (ETM) were built and tested before realization of flight model. The structural model of VHRR payload was subjected to sine vibration, random vibration and shock tests to qualification level (one and half times the level the payload was likely to experience). This model was also subjected to sine/random vibration tests after integration of the payload with structural model of INSAT-2 spacecraft. The inputs derived from

Table 3. Integrated VHRR payload: Performance summary

Parameter	Value 2A VHRR	·Value 2B VHRR
Calibration		
Visible slope/offset	1.08/0.40	1.10/0.31
IR slope/offset	1.30/3.21	1.31/2.36
Vis. Ch. SNR	>9	>8.4
IR Ch. NEDT (K)	<0.15	<0.10
Vis. IFOV (μrad)		
along FS direction	<47	<50
along SS direction	<47	<47
Vis. MTF (%)		
along FS direction	>30	>36
along SS direction	>30	>44
IR IFOV (μrad)		
along FS direction	<188	<195
along SS direction	<163	<155
IR MTF (%)		
along FS direction	>34	>34
along SS direction	>33	>48

these tests were used to update the design of the engineering thermal model. After assembly and performance optimization, this model was tested at the ambient laboratory environment for compliance to the requirements and specifications. The model then underwent qualification level environmental tests which included sine vibration, random vibration and thermal vacuum tests. During thermal vacuum tests the payload performance is evaluated in a 3–metre theromovacuum chamber specially built at the Space Applications Centre, Ahmedabad for testing electro-optical payloads. The tests include evaluation of performance at extremes of temperature in vacuum conditions. The duration of this test was typically about four weeks and temperature excursions on payload closely simulated the transfer orbit conditions and diurnal variations that occur on-orbit. The thermal channel calibration was possible only in thermal-vacuum tests since simulation of thermal radiation from a black-body in the temperature range of 180–340 K is not feasible at ambient environment. After completion of tests at payload level, the instrument was integrated with engineering model spacecraft. The payload was tested along with the spacecraft for sine/random vibration and acoustic input. The payload was subjected to a 21-day thermal vacuum test along with the spacecraft. The spacecraft was also subjected to a solar simulation test to validate the thermal design and VHRR cooler performance under solar illumination conditions. This test was conducted in the large space simulation chamber at the ISRO Satellite Centre, Bangalore.

The flight model of the VHRR instrument after assembly and performance optimization (Figure 9) was subjected to the same set of environmental tests as ETM

INSAT-2A VHRR FCC (VIS/IR,VIS,VIS) 24-SEP-92 11:30

Figure 10. False colour composite of the imagery acquired on 24 September 1992 through INSAT-2A VHRR

but at acceptance test levels. Summary of VHRR flight model performance is shown in Table 3. It may be noted that the summary given here is the worst case values measured during various phases of testing which includes environmental tests.

On orbit performance

The INSAT-2A satellite was launched on 10 July 1992 and it reached the geostationary slot on 27 July. The first pictures of the earth scene imaged by the VHRR

53

INSAT-2B VHRR VISIBLE 31-JULY-93 11:30

INDIAN SPACE RESEARCH ORGANISATION
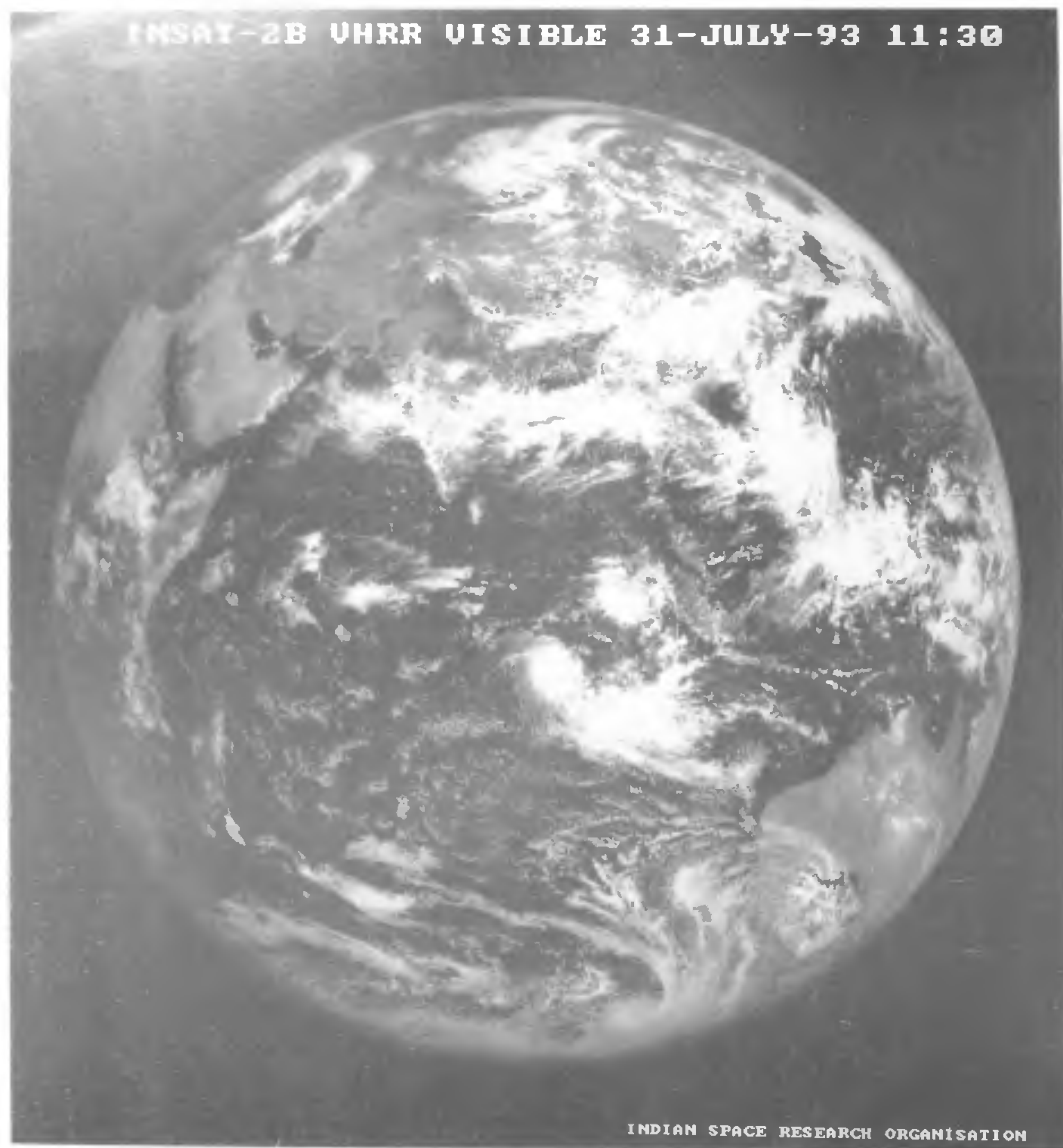
instrument onboard were beamed down on 28 July. A false colour composite image of the earth obtained on 24 September 1992 using INSAT-2A VHRR is shown in Figure 10. The INSAT-2B satellite was launched on 23 July 1993 and it reached its geosynchronous slot by 31 July. The first visible imagery from 2B VHRR was acquired on 31 July at 1130 h and the first IR imagery on 5 August at 1130 h. These imageries are shown in Figure 11 *a*, *b*. Various tests were carried out on

INSAT-2A/2B VHRR payloads to evaluate their performance on-orbit.

Table 4 gives the summary of on-orbit performance. The payload performance on-orbit was evaluated for visible channel signal-to-noise ratio by using the data over uniform reflectance zones from desert and ocean regions. The IR channel calibration check and noise equivalent temperature difference performance were evaluated using data from payload when viewing deep

Figure 11. b. First on-orbit infrared channel imagery acquired through INSAT-2B VHRR on 5 August 1993

Table 4. In-orbit performance of INSAT-2 VHRR

Parameter	Value		
	Specifications	2A VHRR	2B VHRR
Frame-to-frame stability (μrad rms)	< 70	< 34	< 34
IR channel NEDT (scene at 300 K)			
At det. temp. 105 K		0.085 K	0.05 K
At det. temp. 110 K	< 0.25 K	0.125 K	0.065 K
Visible channel detector matching	< 5%	< 4%	< 2.5%
Visible channel SNR (at 2.5% albedo)	> 16	> 11	> 9
Visible channel MTF (at 4 km/cycle)	> 23%	> 35%	> 40%
IR channel MTF (at 16 km/cycle)	> 21%	> 35%	> 35%

space and the onboard black body at different temperatures. The MTF evaluation of visible and infra-red channels were carried out using space-to-earth edge boundaries. The edge response is differentiated and Fourier-transformed to get the MTF.

The VHRR instrument has been generating on an average three full frames and fourteen normal frame images daily. The performance of the instruments has been excellent and they are currently providing valuable input to the India Meteorological Department for their meteorological studies and forecasts on operational basis

1 NASA, the conception, growth accomplishments and future of meteorological satellites, NASA Conf. Publ. 2257, 1980.

2 Gupta, P. P., Rustogi, S. C., Madhuprasad, Dua, H. S. and Basavaraj, A., *J. Spacecraft Technol.*, 1992, **2**, 23–25.

3. VSSC, ISRO Design report on scan mechanism, VSSC-NGC-INSAT, 1986, (ISRO internal report)

On the thermodynamic activities of ions in aqueous solutions of electrolytes

S. Parthasarathy* and K. R. Srinivasan[†]

*Centre for Electrochemical & Energy Research, SPIC Science Foundation, 110, Mount Road, Madras 600 032, India
[†]Institute of Physico Chemical Research, Madras 600 047, India

A strong electrolyte in a dilute aqueous solution of concentration m, completely dissociates into its ions, each individual ion having a concentration m, and each carrying a charge depending on its valency. The thermodynamic activity of each ion will depend on the charge it carries and on m, multiplied by a factor γ termed activity coefficient, to allow for the apparent reduction in concentration caused by mutually interacting different ionic species in the solution. Thus, the activity of an ion in a solution of m may be re-defined as the 'effective strength' of the ion and expressed by the term $z^2 \times m\gamma$, where z is the valency of the ion. It is not the 'effective concentration' or $m\gamma$ as it is now defined and generally assumed to be. Experimental data are presented to confirm this new definition. A reference electrode without liquid junction has been devised to measure single ion activities, using a solid ion-transmitting conductor of silver-chloride rod, which functions as a bridge between the reference and test cells.

Electrode potential, ionic activity and activity coefficient

WHEN a piece of an active metal, like zinc, is dipped in an aqueous solution, the metal acquires a potential, which is a measure of the tendency of the metal to release its ions into the solution and get negatively charged thereby. These ions, as well as the same ions already present in the solution, will tend to annul this tendency of the metal, thereby controlling its potential with respect to the solution. The effectiveness or the strength of an ion in determining the potential of a reversible electrode depends on the concentration of ions of the same kind in the solution and also on the charge carried by the ion. Thus, a doubly-charged ion will be four times as effective as a singly-charged ion in this respect[1]. The strength I_i of an ion in solution is, therefore, a product of its concentration and the square of its valence. However, with increasing concentration of ions in a solution, and with increase in the forces of attraction and repulsion among the charged particles, the free movement of the ion in the solution will be hampered, and its strength reduced to a fraction of its value. Thus, the activity of an ion in a solution of m may be re-defined as the effective strength of the ion expressed by the term $z_i^2 m\gamma_i$ where z_i is the valence of the ion, rather than the effective concentration signified by $m\gamma_i$. This fraction, termed the activity coefficient of the ion, γ_i, is dependent, according to Debye and Huckel, on the ionic strength I of the electrolyte solution as a whole, which takes into account both the concentration and charges of all ions in the solution and in very dilute solutions is given by the relation[2] $-\log \gamma_i = 0.509\, z_i^2 \sqrt{I}$. In the case of solutions of concentrations of about $0.01\, m$, the relation

$$-\log \gamma_i = \frac{0.509\, z_i^2 \sqrt{I}}{1 + \sqrt{I}}$$